RSC Advances

ROYAL SOCIETY OF CHEMISTRY

www.rsc.org/advances

RSC Advances

PAPER

Structural characterization of individual graphene sheets by arc discharge and their growth mechanisms

Received 00th January 20xx,
Accepted 00th January 20xx

DOI: 10.1039/x0xx00000x

www.rsc.org/

Bo Li, Yanli Nan, Peng Zhang and Xiaolong Song*

Graphene sheets by arc discharge are hard to characterize in details due to their complex pristine states in raw soot, which always exhibit an overall morphology of overlapping aggregation, together with other carbonaceous by-products. Here we used an improved arc method and simple separation procedure to obtain a large number of individual graphene sheets with single- to few-layer, and further probed their structural details using optical microscopy, transmission electron microscopy (TEM), atomic force microscopy and Raman spectroscopy. By TEM characterization, two major types of graphene sheets are shown; one is featured as folded fringes and polycrystalline structure, whereas the other is with even graphene plane and single crystalline structure. In contrast to that of supported graphene, Raman spectra of these graphene sheets show some different characteristics such as opposite shift of G band frequency as layer increases. With increasing layer, the frequencies of G and G' bands and the full width at half maximum (FWHM) of G' band totally exhibit layer-dependence. According to the FWHM of G' bands, the folding within graphene sheets is also discussed. In addition, the defect type for arc graphene are analysesd based on the D and D' bands. Our results suggest that the D bands of such graphene sheets result from edges, rather than topological defects or disorder. Based on the findings, a new growth mechanism of arc graphene is proposed rationally responsible for the difference of two types of graphene sheets.

Introduction

The arc-discharge technique to vaporize graphitic carbon via hot plasma opened a new branch of science and technology of nanocarbon materials. Fullerene, especially C_{60} and C_{70}, was first synthesized by a laser evaporation method in 1985, then for the sake of research and mass-production, arc method are developed to prepare this material by Krätschmer et al.[1] Carbon nanotubes (CNTs) were discovered in arc-discharged samples and also developed to meet industrial demands using such arc method.[2] Graphene, a truly two-dimensional nanocarbon, has attracted intensive interest due to its remarkable electronic, thermal, mechanical, and transparent properties.[3] The prevailing synthetic methods used to produce graphene, such as mechanical exfoliation,[4] epitaxial growth,[5] liquid-phase exfoliation,[6] and chemical vapor deposition (CVD),[7] however, basically have inevitable drawbacks in preparation process, transfer techniques, cost, quality or quantity. Arc method is a very promising way to produce high-crystalline, doping-viable, few-defect graphene sheets via simple steps.[8-10] The synthesis of this method is usually carried out under gaseous or liquid background, creating hot plasma to evaporate anode materials. The evaporated carbon radicals (mainly C_2 and C_3 in plasma zone, whereas C_4, C_5... in areas distant from the discharge zone) coalesce and form carbon nanostructures depending on reactive conditions.[11] The central temperature of arc plasma can exceed 4000K, which thermally anneal the products and remove topological defects during the growth process.

The overall morphology of few-layer graphene (FLG) fabricated by arc plasma exhibits infinite as a layer of overlapped sheets without any substrate. Most reported arc FLG sheets have some common structural characteristics as follows: layer number from 10- (10L) to bilayer (2L), lateral size ranging from 100 to 300 nm.[9, 10, 12-17] In arcing process, the kinds of end-products are directly associated with the reactive conditions (buffer gas, catalyst, etc), but the physical dimension and morphology are determined by the process of growth and deposition. People can manipulate arc plasma to control the growth process by adding external magnetic field, resulting in larger-area FLG (500-2500 nm) but with thicker layers of 3-15L.[18, 19] The bottleneck to produce single-layer graphene (SLG) by arc discharge has been successfully solved by virtue of catalysts and rapid cooling, respectively.[13, 20] The former acquired 1-3L graphene sheets in cathode deposit using SiC as carbon source and Cu as catalyst, whereas the latter produced fluffy soot containing 1-3L graphene collected from the inner wall of vacuum chamber.

Arc graphene, and its doped derivatives[21, 22] and hybrids (e.g. Graphene/SnO_2,[23] Graphene/CNTs.[24]) have been demonstrated experimentally to be very applicable for the

State Key Laboratory for Mechanical Behavior of Materials, School of Materials Science and Engineering, Xi'an Jiaotong University, Xi'an 710049, PR China. E-mail: Songxl@mail.xjtu.edu.cn (X. L. Song); Tel: +86 29 82668695; Fax: +86 29 82663453.

†Electronic Supplementary Information (ESI) available: Detailed synthesis methods and parameters, TEM images of samples under varying centrifugal speeds, Raman spectra and comparison plot. See DOI: 10.1039/x0xx00000x

fields of electronic devices, transparent conductive films, supercapacitors, and energy storage due to its high conductivity and specific surface area,[9, 16] high-rate capability,[23] high capacity for hydrogen storage,[25] thermal stability[9, 12] and excellent transparency.[13, 16]

Generally, previous works on the structure and properties of arc graphene are mainly based on aggregated graphene sheets either in raw soot or purified samples. To our knowledge, the structural details of individual graphene sheets, which act as basic units of this material, have barely been reported. However, we could not ignore the structural difference between the ensemble and the individuals. It is well-known that the electronic and band structures of two-dimensional graphene depend strongly on its lateral size, layer number, topological defects, edge types, folding and curvature, which in turn influence directly the properties of the material.[26] For example, arc graphene sheets with lateral size of 100-200 nm have better conductivity and higher rate capability than micro-scale graphene sheets.[23] In addition, we noted that the experimentally measured properties of arc graphene fall within a wide range in the literature.[9, 15, 16, 24] Regardless of synthetic parameters, it is probably associated with the structural details of unit graphene sheets. Therefore, elucidating the detailed characteristics of this type of FLG is required not only for the overall understanding of the structural and properties but also for the development of arc-graphene-based applications. Moreover, the growth mechanism related to their basic units gives people guidelines and new insights into the nature of other nanostructures fabricated by arc plasma, more than nanocarbons.[27]

To this end, we used an improved arc method and simple separation procedure to obtain a large number of individual graphene sheets from single- to few-layer, and further probed their structural characteristics with a combination measurements of optical microscopy, transmission electron microscopy (TEM), high-resolution transmission electron microscopy (HRTEM), atomic force microscopy (AFM) and Raman spectroscopy. Our results exhibit that two major types of graphene sheets with different configurations are formed simultaneously during arcing process. By the observation via TEM and HRTEM, folded fringes are shown as a common feature for the majority of our samples, while the rest are basically ones with even surfaces. These folded fringes formed by curved or bent graphene planes are significantly different from those known for graphene sheets by other top-down methods, such as liquid-phase exfoliation.[6] With increasing layer, arc graphene has an opposite frequency shift of G band compared with supported graphene. Moreover, the frequencies of G and G' bands, as well as the full width at half maximum (FWHM) of G' band totally exhibits layer-dependence. By Raman measurements, the defect types are discussed based on the D band intensity and corresponding intensity ratios. We demonstrated that the D band intensity of arc graphene results from edges, rather than topological defects or disorder. Based on these findings, we proposed a new growth mechanism responsible for the difference of two types of graphene sheets in arcing process.

Experimental Introduction

Briefly, an improved direct-current (DC) arc discharge system with an electric fan centrally faced the discharge zone was employed to carry out the preparation of raw FLG soot. Commercial pure graphite (99.99%) rods of 6 and 15 mm in diameters were set as anode and cathode, respectively. The electrodes were installed horizontally in a high-vacuum closed stainless steel chamber filled with a mixture of helium and hydrogen. Different sets of total pressures of He/H_2 buffer gases were performed ranging from 20-90 kPa in our experiments. The optimized conditions for high fraction of FLG are shown in Fig. S1 of electronic supplementary information (ESI). The direct current was maintained at 90-100 A and discharge voltage was kept at 25-30 V by controlling the gap distance between two electrodes. Raw soot samples were collected from the inner wall of vacuum chamber.

The two-step separation procedures have been carried out by an ultrasonic instrument (DR-MH20, Derui) and a high-speed centrifuge (TGL-16). The solvent contains a mixture of ethanol and deionized water in a volume ratio of 1:4. Due to the negatively charged Si substrate (hydrophilic), the aqueous solution can make the graphene sheets well dispersed.[14] A solution of graphene with concentration of 0.25 mg/mL is processed by 2h sonication and 30 min centrifugation with speeds of 4000, 8000 and 12000 rpm. Then the upper part of solution (supernatant) has been transferred for the following measurements. Fig. S2 in ESI exhibits the TEM images of dispersed graphene sheets under three centrifugal speeds. With the centrifugal speeds from 4000 to 12000 rpm, the dispersion of graphene sheets can achieve a very high level to provide a large number of individual graphene sheets with varying layers.

The bright-field imaging and crystal diffraction of the samples were acquired by employing a TEM (JEOL-200CX) and a HRTEM (JEM-2010F). The acceleration voltages of TEM and HRTEM are 120 and 200 kV, respectively. The size of selected-area aperture is ~200 nm in our experiment. The surface morphology and thickness were probed by an AFM (Innova, Veeco) working at tapping mode on a silicon substrate. Raman spectra were recorded from 1000 to 3500 cm^{-1} using Ar^+ laser excitation wavelength of 514.5nm (HR-800 laser confocal micro-Raman spectrometer, Horiba Jobin Yvon). The instrumental conditions are listed as follows: output: 20 mW, D1 filter; grating: 600 gr×mm^{-1}; objective: ×100, and time: 10s.

Results and discussion

1. TEM and AFM analyses

In Fig. 1a, one can see that arc graphene sheets tangled with each other in raw soot. Fig. 1b illustrates the details of coexisted graphene sheets with varying layers via folded edges. As indicated by the arrows, single- (1L), tri- (3L) and multi-layer graphene sheets are shown clearly according to the folded edges of graphitic (002) planes. By separation process as mentioned in the experimental section, individual graphene

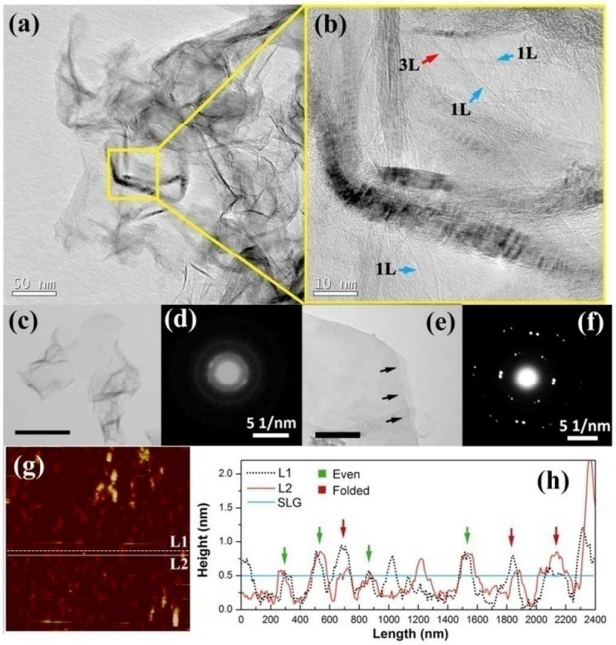

Fig. 1 (a) Arc graphene in raw soot. (b) Magnified image of the box in (a), showing a jumble of single- (1L), tri- (3L) and multi-layer graphene sheets. (c) Typical morphology of an individual graphene sheet with folded fringes. (d) SAED pattern of (c), showing the polycrystalline structure. (e) Typical morphology of an even 2L graphene sheet with clear stacked edges as marked by the arrows. (f) SAED pattern of (e), showing sixfold symmetry and perfect lattice of graphitic structure. The scale bars in (c) and (e) are 200nm. (g) AFM image and (h) height profile show that the height changes of graphene sheets marked by L1 and L2. Green and red arrows denote even and folded graphene surfaces, respectively.

sheets in sufficient quantity can be obtained from the raw soot. Figs. 1c and 1d exhibit the typical morphology of an individual graphene sheet and its selected area electron diffraction (SAED) pattern, respectively. Fig. 1c illustrates the morphology of such individual graphene sheet where a part of the sheet has folded onto itself. According to the figure, the folded parts of graphene are wavy and turbostratic, indicating that the layer stacking is not commensurate and disordering, possibly because of the uncontrolled growth process and the presence of other non-six-member carbon rings. The detailed growth mechanism will be discussed below. We found that the diffraction spots are weak and tend to be rings, indicating that the polycrystallinity of this graphene sheet. The innermost spots correspond to a lattice spacing of 0.37 nm in the real space, larger than the 0.334 nm in graphite, denoting the changes of graphene lattice. As shown in Fig. 1e, another typical graphene sheet has a relatively even surface with clear stacked edges as marked by the arrows. Fig. 1f exhibits the SAED pattern of the graphene sheet as depicted in Fig. 1e. The bright and sharp spots indicate the sixfold symmetry of six-member carbon rings in basal plane, as well as the perfect lattice of this graphene sheet. Each set of diffraction spots in the same site is different in intensity, which indicates that the present graphene sheet is formed by the stack of two component layers with different thickness.[28] The angle between the neiborghing spots means these component layers stacked at a rotational degree of ~6°. Diffraction spots with sixfold rotational symmetry show that electrons are incident normal to the basal plane of crystal based on six-member carbon rings, allowing us to label the spots with the Miller-Bravais indices (hkil). The innermost six spots correspond to the (10-10) set of lattice planes in the real space with a lattice spacing of 0.214 nm, and the outer spots correspond to the (11-20) set of planes with lattice spacing of 0.126 nm. Both lattice parameters are in agreement with the counterpart values of 0.213 and 0.123 nm of mechanically exfoliated SLG.[29] Fig. 1g is the AFM overview image of our sample within an area of 2.4×2.4 μm^2, showing good dispersion of these graphene sheets. The corresponding height profiles of L1 and L2 in Fig. 1g are shown in Fig. 1h, reflecting the height variation of the same graphene surfaces. The height curves indicated by green arrows mean graphene sheets with even surfaces, while the rest marked by red arrows denote those graphene sheets with uneven surfaces, further proving that the presence of folded structure. In addition, the mean thicknesses of 1L and 2L graphene sheets are about 0.5 and 0.9 nm, respectively.

As seen in Figs. 2a to 2d, HRTEM images illustrate the folded edges of 1L to 4L graphene sheets, respectively. In Figs. 2a and 2c, very even surfaces of graphene planes (SLG and trilayer) indicate the high quality and perfection of graphene sheets fabricated by arc plasma. In contrast, some of these graphene sheets are shown as bent and uneven surfaces of basal planes, indicating the formation of some topological defects during the growth process, as shown in Fig. 2b and 2d. In addition, a special structure is also observed (Fig. 2e), which resembles the overlapped crease in multilayer graphene system, including pure and skewed stacking configurations.[30] Fig. 2f plots the relationship between interlayer spacing, d, and layer number, n of arc graphene. Obviously, a relaxation of van der Waals's interaction between two neighboring layers (n≤10) occurs since the interlayer spacing of 10L to 2L graphene

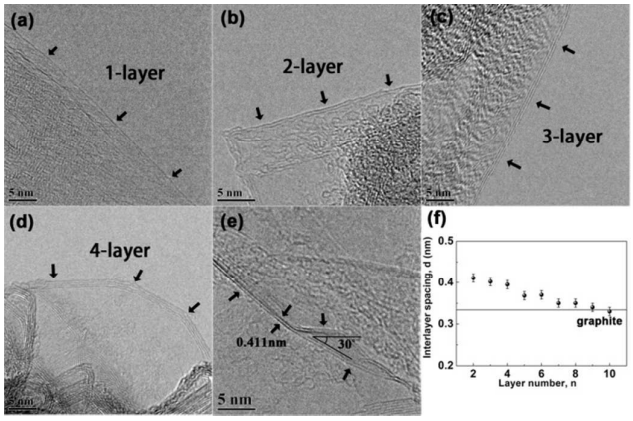

Fig. 2 (a)-(d) HRTEM images of folded edges of 1L to 4L graphene sheets, showing the presence of even and bent graphene basal planes within the samples. (e) A crease-like structure in a 3-layer graphene system with the angle of 30°. (f) The plot of interlayer spacing, $d_{(002)}$, vs layer number, n, indicating the relaxation of interlayer bonding force. The line indicates the $d_{(002)}$ value of 0.334 nm for bulk graphite.

increases from 0.34 to 0.41 nm. Hence only graphene sheets with layer number less than 10L can be defined as "few-layer" graphene.

2. Raman spectra of individual graphene sheets

In the last decade, extensive research on Raman scattering of graphene has firmly established that the lineshape and the FWHM of G' band, as well as the intensity ratio of $I_{G'}/I_G$, are unambiguously indicative of layer number of graphene, especially for mechanically exfoliated graphene.[31] In previous works, a large number of mechanically exfoliated AB-stacked graphene samples with micron sizes show substantial and distinguishable ranges of FWHM of G' bands for single-, bi- and tri-layer graphene at 27.5±3.8 cm^{-1}, 51.7±1.7 cm^{-1}, and 56.2±1.6cm^{-1}, respectively.[32] As shown in Fig. S3 of ESI, however, arc graphene sheets, whose lateral sizes are much smaller than that of mechanically exfoliated graphene, even smaller than the laser spot size (~1μm) in Raman measurement, exhibit different but also straightforward features for determining the layer number. According to the contrast of optical transparency and corresponding FWHM of G' band, we can evaluate the layer number accurately. In our studies, graphene with single-layer is almost transparent in optical observation and its lineshape symmetry, the $I_{G'}/I_G$ ratio (~1.2) and FWHM of G' band (~42cm^{-1}) are consistent with that of liquid-phase exfoliated SLG sheet (~300nm in size, $I_{G'}/I_G$ ~1.5, FWHM ~42cm^{-1}).[33] Hence this is a solid evidence to demonstrate the accuracy of such assessment for layer number used in this work.

The optical microscopy image and typical Raman spectra of individual graphene sheets with layers of 1-3L are shown in Figs. 3a and 3b, respectively. In particular, the values of I_D/I_G ratio, $I_{G'}/I_G$ ratio and FWHM of G' bands are also listed accordingly in Fig. 3b. At 514.5nm excitation, three major bands of G, D and G' are always shown in Raman spectra of graphitic and graphene materials. G band (~1582 cm^{-1} for graphite) is a prominent feature for graphitic materials, which corresponds to the high-frequency E_{2g} phonon at the center (Γ point) of Brillouin zone (BZ).[34] That is, G band is related to the in-plane vibration of graphene basal plane whose crystalline quality can be assessed by the FWHM of G band. The origin of D band (~1350 cm^{-1}) is related to the phonons of transverse optical (TO) branches around the corner of K point in BZ, activated by an intervalley double resonance (DR) process and dispersed strongly with excitation energy due to Kohn anomaly at K.[35] The D band is associated with the A_{1g} breathing modes of six-member carbon rings, which requires defects or disorder for its activation.[34] Another prominent feature appearing at approximately 2700 cm^{-1} for 514.5 nm laser excitation is called G' band, which is also known as 2D band in the literature. The second-order G' band in SLG arises from a DR process involving intervalley scattering by two iTO phonons.[36] This DR process gives rise to an intense G' band and larger than G band in intensity.

In this work, G band frequency, ω_G, downshifts by approximately 5cm^{-1} in SLG sheet, i.e. $\omega_G(1)$ ~1577 cm^{-1} (See in Fig. 3b). That is, ω_G increases with the increasing layer number, showing slight variation in frequency ($\Delta\omega_G$~5cm^{-1}). Thus the near linear layer-dependence can be presented as $\omega_G(n)=\omega_G(\text{graphite})+\beta/n$, where β≈–4.78 cm^{-1} is a constant. Interestingly, we found that the frequencies of G bands in our samples are shown as an opposite shift (blue-shift) compared to supported graphene films, whose ω_G decreases (red-shift) as layer number increases.[37] As mentioned above, Raman scattering of G band is related to in-plane vibrations, thus the shift of ω_G is most likely due to the changes of relative motions of in-plane carbon atoms. Doping, charged impurities or strain can lead to a blue or red shift of G band due to the change of C-C distance.[37-39] The $\Delta\omega_G$ values in the cases of doped charges and strain can reach a maximum of ~9 cm^{-1} and ~5-6 cm^{-1}, respectively.[38, 39] Because of the universality of ω_G shift for arc graphene, as well as the nature of arc plasma, we inferred that the ω_G shift results from the external charges, which extensively exist within the arc plasma.[40, 41] As layer increases, the absorption of external charges is eliminated because of the recovery of normal stacking order of graphitic layers.

In Fig. 3b, the D' band split as a shoulder of G peak is caused by an intravalley DR process, which is associated with graphite or graphene edges, or reduction in grain size.[42-44] As for individual 1-3L graphene sheets, the D' bands are always obvious and easy to identify. With the increasing layer, the D' band gradually merges into G band. In raw soot sample and starting graphite, the D' bands almost disappear due to the aggregation of samples. In Fig. S4 of ESI, a weak peak appearing at ~1450 cm^{-1} is observed between D and G bands in Raman spectra of some graphene sheets by accident. There are two explanations for the presence of this band in the literature; one is the third order signals of silicon substrate,[43] while the other is due to defect scattering.[37] These so-called D-scattering D_2 and D_3 bands are also shown in supported n-graphene layer films.

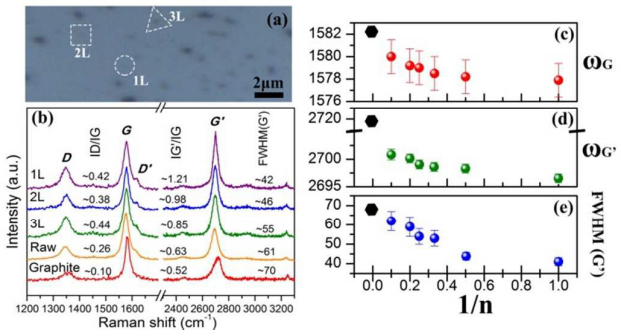

Fig. 3 (a) Optical microscopy image of well-dispersed graphene sheets. (b) Typical Raman spectra of individual 1-3L graphene sheets, raw graphene soot and starting graphite excited by 514.5 nm laser excitation. The corresponding values of ID/IG, IG'/IG and FWHM of G' bands are also listed. (c-e) show the average values of G band frequency (ωG), G' band frequency (ωG'), and the FWHM of G' band as a function of the inverse of layer number (1/n), respectively. The black solid hexagon indicates the values of bulk graphite.

In contrast to the narrower FWHM of G' band for mechanically exfoliated SLG (~24 cm^{-1}), we note that the FWHM for arc SLG is wider (~41.5 cm^{-1}), indicating the broadening of G' band, which also occurs in other graphene sheets with similar size.[33] This is owing to symmetry lowering, which relaxes the selection rules for Raman scattering. Importantly, the information of G' band is sensitive to layer number because its Raman mechanism is closely related to the electronic band structure, which is changed with layer number and relative orientation.[31] In our samples, with increasing layer, the frequency of G' band increases (blue-shift) and the FWHM becomes broader (See in Fig. 3c and 3d). The specific values of FWHM of G' bands for 1-3L graphene are 41.2±1.4 cm^{-1}, 46.4±1.6 cm^{-1}, and 55.1±1.5cm^{-1}, respectively. Both the trends of frequency and FWHM for G' band are consistent with the results in the literature.[36]

The overtones of 2D' band centred at ~3240 cm^{-1} originates from a process with momentum conservation, which is satisfied by two phonons with opposite wavevectors. Both G' and 2D' bands always exist regardless of defects.[31] Additional weak bands in the high-order region (ω ~2450 and ~2950 cm^{-1}) are assigned as D+D" and D+D', respectively. D" derives from a phonon belonging to the longitudinal acoustics (LA) branch, seen at ~1100 cm^{-1} for visible excitation in defected samples.[34] This mode is probably associated with contributions from region near K point of the BZ boundary, and becomes Raman active due to the selection-rule relaxation resulting from defects. In addition, the D+D' band is the combination of phonons with different momenta, around K and Γ, also requires a defect for its activation.[34] In Fig. 3b, it is clear that the 2D', D+D" and D+D' bands are relatively stable in both position and intensity.

As for folded and even graphene sheets, three typical Raman spectra of SLG, bilayer graphene and folded SLG are shown in Fig. 4a. The G band of bilayer sample becomes more intense than even and folded SLG due to more carbon atoms contributing to this vibration mode under laser irradiation. The determination of folding within graphene also depends upon the symmetry and FWHM of G' band. Due to arbitrary stacking, the G' band of folded SLG exhibit slight position shift, lineshape asymmetry and larger FWHM (~50cm^{-1}) than that of bilayer graphene (~46cm^{-1}), but smaller than that of trilayer (~55cm^{-1}) (See the inset of Fig. 4a). For even SLG, the G' band can be fitted into only one Lorentzian peak (Fig. 4b), which represents the single π electron valence band and π* conduction band structure, and thus only one DR scattering cycle is excited near the K and K' points (Fig. 4c). A whole DR cycle involves the four processes as follows: i) laser-induced excitation of electron (e-) — hole (h+) pair; ii) scattering (the first resonance process), and iii) back-scattering of the excited electron (the second resonance process) by two phonons with opposite wavevectors q and –q; iv) the recombination of electron-hole pair. As shown in Fig. 4d, the G' band for bilayer sample is dispersive and can be fitted into four Lorentzian peaks. In bilayer system, the interaction between two layers causes the π and π* bands to divide into four parabolic band structures as π_1, π_2, π_1* and π_2*. Therefore, four Raman scattering cycles occur and their DR processes are denoted by the lines with two arrowheads in different colors in Fig. 4e. Each line represents a whole DR process. For multilayer system (≥3L), the electronic bands split into more complex and dispersive configurations, thus excited electron-hole pairs are involved in more scattering cycles, which contribute to a broader G' band. In folded SLG, the G' band has a similar

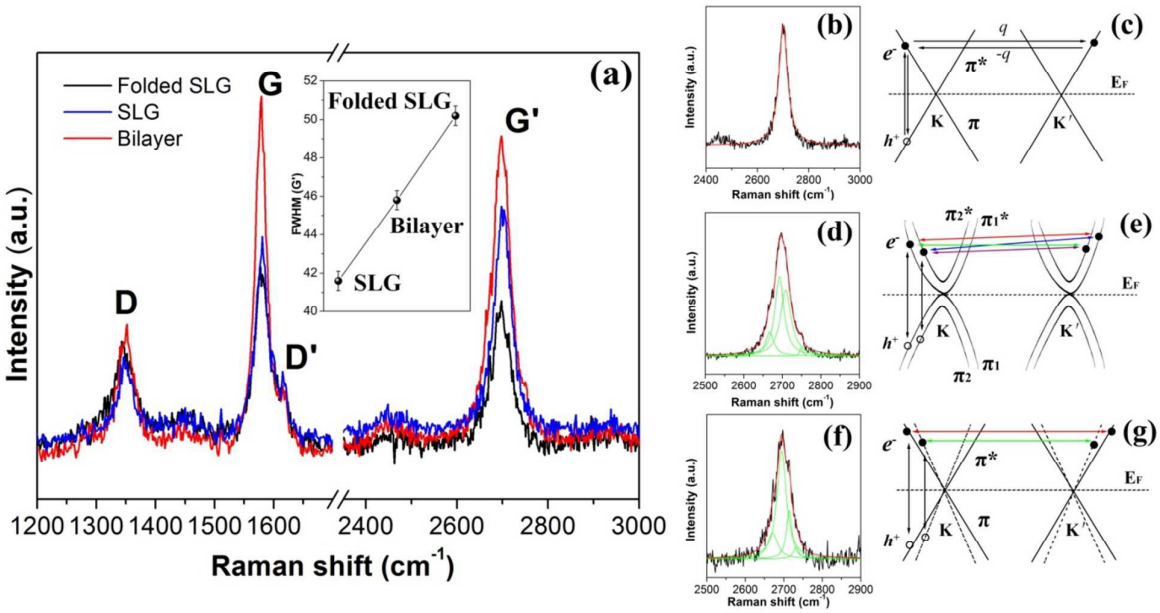

Fig.4 (a) Typical Raman spectra of SLG, bilayer graphene and folded SLG. (b) The single-Lorentzian fitted lineshape of G' band of SLG, and (c) its DR mechanism of Raman scattering. (d) The fitted four components of the G' band of bilayer graphene, and (e) the corresponding DR mechanism. (f) The fitted four components of the G' band of folded SLG, and (g) the corresponding DR mechanism.

frequency position to that of even SLG, but downshifts 4cm^{-1} compared to that of bilayer sample. The change of G' position for folding part is also opposite compared with that of micron-sized graphene by mechanical exfoliation.[32] That indicates the folded SLG exhibit a similar electronic structure to SLG but with increased Fermi velocity, which cause a larger slope of electronic band near K (K') points, as illustrated in Fig. 4g. Previous studies show that misoriented bilayer graphene exhibit that electronic structures are similar to those of SLG but with reduced Fermi velocity, which means a smaller slope of dispersion curve near the K or K' points.[45] With regard to the opposite frequency shift, we still consider linear π electron bands to explain its Raman scattering mechanism, as shown in Fig. 4g. The phonon with smaller wavevector q' couples the Raman process that corresponds to a reduced slope of electronic sub-bands (dash lines), and thus lower frequency phonon dispersion near K points contributes to the G' band.

The intensity ratio of D/G bands, I_D/I_G, is widely used for characterizing the nanographite size L_a in graphitic materials. An empirical relation proposed by Tuinstra and Koenig (T-K) has been used as calibration for the qualitative control of structural transformation of graphitic materials.[46] The inverse of L_a is defined as defect density, n_D, which is used to denote quantitatively the degree of initial defects. Prior to discuss the intensity ratio I_D/I_G of our sample, L_a and L_D, which are frequently encountered in the literature, should be carefully distinguished. Basically, the measure of L_a depends on the amount of disorder in a nanocrystallite given by the amount of one-dimensional border with respect to total crystallite area. While the latter, L_D, denotes the distance between defects in graphene with zero-dimensional point defects. Therefore, L_a is suitable for line defects or polycrystalline graphene with domains, whereas L_D is more appropriate to describe the density of point-like defect within graphene. The correlations between L_D (n_D) and I_D/I_G are depicted as follows:[47]

$$L_D^2\left(nm^2\right)=\frac{(4.3\pm1.3)\times10^3}{E_L^4}\left(\frac{I_D}{I_G}\right)^{-1} \quad (1)$$

$$n_D\left(cm^{-2}\right)=(7.3\pm2.2)\times10^9E_L^4\left(\frac{I_D}{I_G}\right) \quad (2)$$

where E_L is laser energy, and equals 2.41 eV for 514.5 nm laser wavelength. Note that Equations (1) and (2) are only valid for graphene samples with point defects separated by $L_D \geq 10$nm using excitation light in the visible range.[47]

According to HRTEM observations, the contributions to defect-induced D mode are hardly to distinguish because the possible defects within this material include edge-like defects, topological defects (point defect, line defect), and fold-induced defects. Especially, folding may introduce more complex structural changes such as interlayer misorientation, and the bending or curvature of basal planes, which totally influence the Raman scattering process. To simplify the scenarios, the roles of each defect type in the contribution to D mode are discussed below separately. First, point defect is assumed to be the sole defect type in SLG, and then the L_D is in the range from 13.7 to 18.8 nm according to Equation (1). Compared to the order of magnitude of these graphene sheets in size (~260 nm), the value of L_D indicates very low density of point defects and its contribution to D mode could be negligible. Similarly, without consideration of Raman relaxation length for point defect, a line defect can be seen topologically as a combination of some point defects, hence the low density of point defect will not lead to the massive presence of line defects. Second, as for fold-induced defects, Raman signatures caused by strongly folding (superlattice) will generate an additional I band at ~1358cm^{-1} with respect to D band,[48] or even a new R' band centered at ~1625cm^{-1}.[49] Moreover, the fold-induced enhancement of D band intensity is only shown in SLG system, i.e., between perfect SLG and folded SLG regions. In FLG system, however, the impact of folding on D mode is negligible.[50] These results strongly imply that the fold within arc graphene contribute little to D band intensity even though it leads to a broader FWHM of G' band. Third, due to massive presence of graphene edges, we inferred that the edges may play important role in the contribution to D bands. To validate this thought, three groups of measurements on the absolute intensities of D bands of graphene sheets with different numbers (N) are designed, as shown in Fig. 5a. Specifically, the cases as displayed in red (i), blue (ii) and green (iii) indicate the measurements on individual (N=1), two (N=2), three (N=3) graphene sheets under laser irradiation, respectively. The laser spot size is jointly determined by excitation wavelength, λ, and effective numerical aperture, N.A. In this work, the laser spot size is about ~1μm. Fig. 5b exhibit the Raman spectra of the as-mentioned cases (i, ii, iii) and a reference Raman spectroscopy (black) measured on non-separated sample (N>20) which occupy the whole area of laser spot. For N=1 samples, that is, individual graphene sheets, including 1L, 2L and 3L, totally

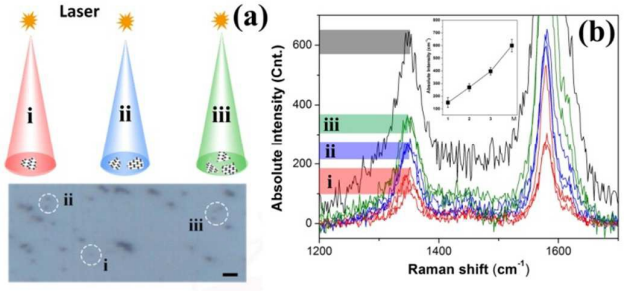

Fig. 5 (a) Schematic of Raman measurements on individual to multiple graphene sheets and the corresponding optical microscopy image (scale bar: 1μm). i, ii and iii denote the cases of one (N=1), two (N=2) and three (N=3) graphene sheets, respectively. (b) Typical Raman spectra exhibit the absolute intensities of D bands of individual to multiple graphene sheets. The red, blue and green curves were taken according to the cases of i, ii and iii in (a), respectively. The black curve corresponds to the case of multiple graphene sheets (N>20) which occupy the whole area of laser spot. The inset in (b) gives the relationship between the mean absolute intensities of D bands and the sheet number (N), showing edge-dependent changes of D-band intensities.

show similar D intensities but increased G intensities due to increasing carbon atoms. In this case, the measured samples show a near constant D band intensities (~143±35 cnt.) but varying G band intensities, revealing that no obvious variance of D band intensity with regard to layer number for individual graphene sheets. Moreover, the stable D intensity probably indicates that the fold-induced structural changes have little contribution to D band scattering. In the scenario of case (ii) (N=2), adding one graphene sheet result in near twice larger intensity of D band than that of case (i), equalling about 275± 30 cnt. Similarly, the D band intensity of three graphene sheets (N=3) is approximately 381±28 cnt. For non-separated sample (N>20), the D band intensity achieve to above 600 cnt, much of which is probably due to the stacking disorder, rather than edges. As expected, the changes of D band intensities are shown as a near linear relationship with respect to increased sheet number, N. (the inset of Fig. 5b). Therefore, edge-like defect is rationally considered as a dominant factor to D mode for arc graphene sheets.

On the other hand, the formation of defects and their types depend crucially on the process of crystal growth. For example, boundaries are always shown in the CVD-grown polycrystalline graphene because simultaneous nucleation at different locations lead to independent domains, then a boundary appears when two neighbouring domains coalesce. In arcing process, high temperature (>4000 K) in plasma zone facilitates the relaxation toward thermal equilibrium, and defects can anneal rapidly. Because of high formation and migration energies of point defects, it is unlikely that there are any new vacancies or adatoms after growth.[51]

In addition, D' band is also indicative of defects in graphene. As documented, the intensity ratio of D and D' bands, $I_D/I_{D'}$, is strongly associated with the nature of defect on graphene surface.[52] The $I_D/I_{D'}$ ratio depends on the type of defects, with edge-like or boundary defects being characterized by $I_D/I_{D'}$ ~3.5, whereas point-like defects (vacancy) in graphene basal plane giving rise to $I_D/I_{D'}$ ~7 and sp^3-hybrized defects to ~13.[52] As shown in Fig. 6, the intensity ratio of I_D/I_G as a function of $I_{D'}/I_G$ indicates that the values of $I_D/I_{D'}$ of 1L to multi-layer graphene sheets basically fall within the range between edge and point defects. From FLG to graphite, basal plane defects or disorder contribute largely to D mode, rather than edges. Moreover, the mean $I_D/I_{D'}$ value of 1L (~4) to 2L (~4.1) graphene sheets strongly suggest that very low density of point defects in basal plane of such FLG sheets. We also noted that some of $I_D/I_{D'}$ data for 3L and multilayer graphene are distributed in the vicinity of vacancy line (~7), indicating that the possible presence of multi-type defects. Moreover, the Raman scattering processes of multilayer graphene, including 3L, are more complex than that of 1L or 2L graphene. Hence the $I_D/I_{D'}$ indicator may not be very accurate for thicker graphene. As for 1L or 2L graphene, their $I_D/I_{D'}$ data full within the range of edge-like defect, which are in good agreement with the above discussion.

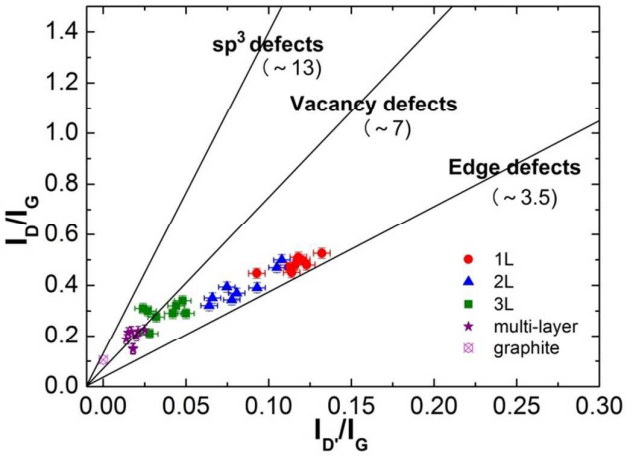

Fig. 6 The intensity ratio of ID/IG as a function of ID'/IG, showing that the defect type of 1L and 2L full within the range of edge defects. For 3L or multilayer graphene (>3L), some of ID/ID' data are distributed in the vicinity of vacancy line (~7), indicating that the possible presence of multi-type defects within this material.

Mechanically exfoliated graphene is always used as an ideal sample to investigate the intrinsic properties of graphene due to its defect-free lattice and Bernal stacking. Actually, edge or boundary should be taken into consideration for most graphene samples such as CVD-grown graphene, graphene sheets and nanoribbons. For arc graphene sheets, small lateral size leads to massive presence of edges within the material, thus the properties is probably different from that of large-area supported graphene. As shown in Fig. S5 of ESI, graphene sheets fabricated by techniques of liquid-phase exfoliation,[33, 53-56] reduction of graphene oxide[57, 58] and arc discharge,[10, 12-17, 19] always exhibit lower $I_{G'}/I_G$ ratios, broader FWHM of G' bands, and the presence of D band in contrast to mechanically exfoliated SLG.[31] That indicates the electronic and vibrational properties of such graphene sheets have been changed by finite lateral size and massive edges. Moreover, the structural quality of arc graphene is comparable with that of liquid-phase exfoliated graphene, and superior to that of reduced graphene oxide.

3. Growth mechanism of arc graphene

High temperature and arc force are two major factors in the growth of carbon nanomaterials. High temperature will lead to the evaporation of graphitic anode, resulting in carbon clusters with various atomicities. The arc forces usually consist of electromagnetic force (denoted as P_r in Fig. 7a), spot pressure and plasma fluid force.[40, 41] Specifically, the former two forces are related to the ionization of gas molecules, as well as the evaporation and exfoliation of anode, whereas the last one supplies gas molecules into arc zone and pushes the ionized and evaporated matters into the ambient space, as shown in Fig. 7b. It is well known that the formation of CNTs and fullerene by arc discharge is crucially dependent on the presence of non-six-member carbon rings, which are indispensable for the curling/rolling of graphene planes.[11] On

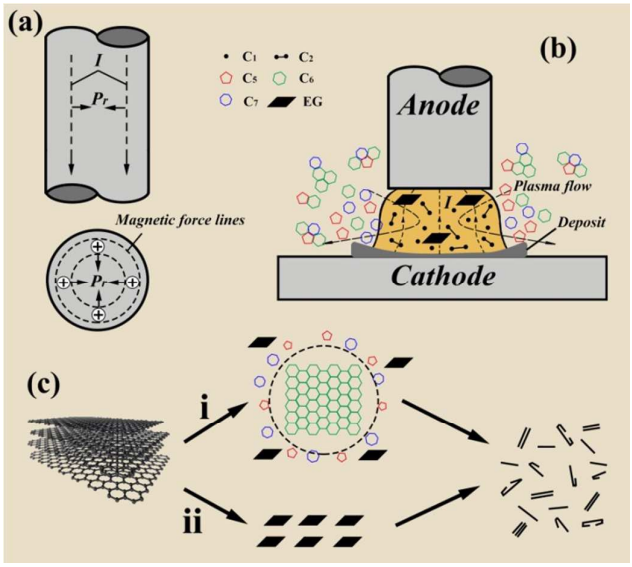

Fig.7 Schematic of growth mechanism of arc graphene with two different structures. (a) Side and cross-sectional views of carbon anode when generates arc force. I and Pr denote the electric current and electromagnetic force, respectively. (b) Recombination of carbon clusters with varying atomicities. Red, green and blue circles denote the pentagon, hexagon and heptagon of carbon atoms, respectively. EG means directly exfoliated graphene from the anode. (c) Two synthetic routes of graphene sheets in arcing process: i) non-six-member carbon rings bond EG together. The dash circle illustrates the "hinge" effect of non-six-member carbon rings. ii). The rest EG sheets directly deposit onto the chamber wall.

the other hand, the production of arc graphene on the chamber wall is widely believed due to the direct exfoliation of graphitic layers from the carbon anode.[9, 12, 13] In this work, however, we observed that two major types of graphene sheets coexist within the soot collected from the chamber wall, indicating the different mechanism compared with the previously proposed mechanism of arc graphene growth. That is, graphene sheets on the chamber wall result from the direct exfoliation of graphitic anode due to the arc or gas pressure.[12] As shown in Fig. 7c, we inferred that two synthetic routes are probable for the graphene growth in arcing process: i) Non-six-member carbon rings, including carbon pentagon (C_5) and heptagon (C_7), bond the exfoliated graphene (EG) together due to the presence of dangling bonds and introduce curvature. The dash circle illustrates the "hinge" effect of non-six-member carbon rings. Hence, the products grown in this way show poly-crystallinity as observed by TEM. (ii) EG sheets are directly from the exfoliation of graphitic anode, keeping their integrity of graphene lattice in the whole process, which is also demonstrated by the TEM observation.

Conclusions

Raw soot containing high-percentage of FLG sheets are synthesized using an improved arc discharge under optimized conditions of rapid-flow and buffer gas. Simple separation procedures enable such raw soot to eliminate most carbonaceous by-products and be well dispersed in graphene suspension. TEM and HRTEM observations show that two major types of graphene sheets coexist within the samples; one is featured as folded fringes and polycrystalline structure, whereas the other is with even graphene plane and single crystalline structure. The folding configuration of graphene surfaces are also probed by AFM measurements, which demonstrate the presence of even and folded graphene sheets according to varying heights. In Raman measurements, both frequency and FWHM of G' band exhibits good layer-dependence, which is in agreement with that for supported graphene. The G frequency, however, is presented as an opposite red-shift from graphite (1582 cm^{-1}) to SLG sheet (1577 cm^{-1}) in contrast to supported graphene films. The G-frequency shift probably results from the presence of excessive charges induced by arc plasma. In addition, the G' band of folded SLG sheet shows broader FWHM than that of bilayer graphene, but similar position to that of even SLG, indicating that their different Raman scattering mechanisms related to DR models. Moreover, we demonstrated experimentally the D band of individual graphene mainly results from edge-like defects, rather than topological defects or disorder. This is evidenced by incremental absolute D intensities as the amount of graphene sheets increases under identical experimental conditions. The results of $I_D/I_{D'}$ analysis also implies that edge-like defects are dominant for 1-3L graphene sheets. The comparison of graphene sheets by different methods, i.e. arc graphene, liquid-phase exfoliated graphene and reduced graphene oxide, shows that the high quality of our samples. Based on the findings, a new growth mechanism of arc graphene is proposed rationally responsible for the difference of two types of graphene sheets. According to the nature of arc plasma and the presence of non-six-member carbon rings, two synthetic routes occur simultaneously during arcing process. One type of single crystal graphene with even surface is exfoliated directly from graphite anode by arc force, whereas the other type of graphene with folded and polycrystalline structure is the combination of some small sheets linked by non-six-member carbon rings in arc growth zone. In a word, our studies show that the structure of arc graphene is inhomogeneous in details even though the samples are synthesized under identical conditions, which in turn leads to process control of arc plasma synthesis.

Acknowledgements

This work was financially supported by the Natural Science Foundation of Shaanxi Province and the Doctoral Research Assistant Foundation of Xi'an Jiaotong University. B. Li was personally supported by the Fundamental Research Funds for the Central Universities.

Notes and references

1. W. Kratschmer, L. D. Lamb, K. Fostiropoulos and D. R. Huffman, *Nature*, 1990, **347**, 354-358.

2. Y. J. Su and Y. F. Zhang, *Carbon*, 2015, **83**, 90-99.
3. K. S. Novoselov, V. I. Fal'ko, L. Colombo, G. P. R., M. G. Schwab and K. Kim, *Nature*, 2012, **490**, 192-200.
4. K. S. Novoselov, A. K. Geim, S. V. Morozov, D. Jiang, Y. Zhang, S. V. Dubonos, I. V. Grigorieva and A. A. Firsov, *Science*, 2004, **306**, 666-669.
5. C. Berger, Z. Song, X. Li and X. Wu, *Science*, 2006, **312**, 1191-1196.
6. Y. Hernandez, V. Nicolosi, M. Lotya, F. M. Blighe, Z. Y. Sun, S. De, I. T. Mcgovern, B. Holland, M. Byrne, Y. K. Gun'ko, J. J. Boland, P. Niraj, G. S. Duesberg, S. Krishnamurthy, R. Goodhue, J. A. Hutchison, V. Scardaci, A. C. Ferrari and J. N. Coleman, *Nature nanotechnology*, 2008, **3**, 563-568.
7. X. Li, W. Cai, J. An, S. Kim and J. Nah, *science*, 2009, **324**, 1312-1314.
8. N. Li, Z. Y. Wang, K. K. Zhao, Z. J. Shi, Z. N. Gu and S. K. Xu, *Carbon*, 2010, **48**, 255-259.
9. Z. S. Wu, W. C. Ren, L. B. Gao, J. P. Zhao, Z. P. Chen, B. L. Liu, D. M. Tang, B. Yu, C. B. Jiang and H. M. Cheng, *ACS nano*, 2009, **3**, 411-417.
10. K. S. Subrahmanyam, L. S. Panchakarla, A. Govindaraj and C. N. R. Rao, *Journal of Physical Chemistry C*, 2009, **113**, 4257-4259.
11. H. Lange, A. Huczko, M. Sioda and O. Louchev, *Journal of nanoscience and nanotechnology*, 2003, **3**, 51-62.
12. R. Kumar, R. K. Singh, P. K. Dubey, P. Kumar, R. S. Tiwari and I. K. Oh, *J Nanopart Res*, 2013, **15**.
13. L. P. Huang, B. Wu, J. Y. Chen, Y. Z. Xue, D. C. Geng, Y. L. Guo, G. Yu and Y. Q. Liu, *Small*, 2013, **9**, 1330-1335.
14. B. S. Shen, J. J. Ding, X. B. Yan, W. J. Feng, J. Li and Q. J. Xue, *Appl Surf Sci*, 2012, **258**, 4523-4531.
15. Y. N. Chen, H. B. Zhao, L. M. Sheng, L. M. Yu, K. An, J. Q. Xu, Y. Ando and X. L. Zhao, *Chem Phys Lett*, 2012, **538**, 72-76.
16. Y. P. Wu, B. Wang, Y. F. Ma, Y. Huang, N. Li, F. Zhang and Y. S. Chen, *Nano Res*, 2010, **3**, 661-669.
17. Z. Y. Wang, N. Li, Z. J. Shi and Z. N. Gu, *Nanotechnology*, 2010, **21**.
18. J. Li, A. Shashurin and M. Keidar, *Ieee T Plasma Sci*, 2011, **39**, 2366-2367.
19. I. Levchenko, O. Volotskova, A. Shashurin, Y. Raitses, K. Ostrikov and M. Keidar, *Carbon*, 2010, **48**, 4570-4574.
20. B. Li, X. L. Song and P. Zhang, *Carbon*, 2014, **66**, 426-435.
21. B. S. Shen, J. T. Chen, X. B. Yan and Q. J. Xue, *Rsc Adv*, 2012, **2**, 6761--6764.
22. S. A. Shah, L. Cui, K. Lin, T. Xue, Q. Guo, L. Li, L. Zhang, F. Zhang, F. Hu, X. Wang, H. Wang, X. Chen and S. Cui, *Rsc Adv*, 2015, **5**, 29230-29237.
23. Z. Y. Wang, H. Zhang, N. Li, Z. J. Shi, Z. N. Gu and G. P. Cao, *Nano Res*, 2010, **3**, 748-756.
24. Y. P. Wu, T. F. Zhang, F. Zhang, Y. Wang, Y. F. Ma, Y. Huang, Y. Y. Liu and Y. S. Chen, *Nano Energy*, 2012, **1**, 820-827.
25. G. F. Guo, H. Huang, F. H. Xue, C. J. Liu, H. T. Yu, X. Quan and X. L. Dong, *Surf Coat Tech*, 2013, **228**, S120-S125.
26. P. T. Araujo, M. Terrones and M. S. Dresselhaus, *Materials Today*, 2012, **15**, 98-109.
27. J. Yu, J. Gao, F. H. Xue, X. Yu, H. Yu, X. Dong, H. Huang, A. Ding, X. Quan and G. Cao, *Rsc Adv*, 2015, **5**, 68714-68721.
28. S. Horiuchi, T. Gotou, M. Fujiwara, T. Asaka and T. Yokosawa, *Applied physics letters*, 2004, **84**, 2403-2405.
29. J. C. Meyer, A. K. Geim, M. I. Katsnelson, K. S. Novoselov, D. Obergfell, C. Roth, C. Girit and A. Zettl, *Solid State Commun*, 2007, **143**, 101-109.
30. A. W. Robertson, A. Bachmatiuk, Y. A. Wu, F. Schaffel, B. Buchner, M. H. Rummeli and J. H. Warner, *ACS nano*, 2011, **5**, 9984-9991.
31. A. C. Ferrari, J. C. Meyer, V. Scardaci, C. Casiraghi, M. Lazzeri, F. Mauri, S. Piscanec, D. Jiang, K. S. Novoselov, S. Roth and A. K. Geim, *Physical review letters*, 2006, **97**, 187401.
32. Y. Hao, Y. Wang, L. Wang, Z. Ni, Z. Wang, R. Wang, C. K. Koo, Z. Shen and J. T. Thong, *Small*, 2010, **6**, 195-200.
33. K. R. Paton, E. Varrla, C. Backes, R. J. Smith, U. Khan, A. O'Neill, C. Boland, M. Lotya, O. M. Istrate, P. King, T. Higgins, S. Barwich, P. May, P. Puczkarski, I. Ahmed, M. Moebius, H. Pettersson, E. Long, J. Coelho, S. E. O'Brien, E. K. McGuire, B. M. Sanchez, G. S. Duesberg, N. McEvoy, T. J. Pennycook, C. Downing, A. Crossley, V. Nicolosi and J. N. Coleman, *Nature materials*, 2014, **13**, 624-630.
34. A. C. Ferrari and D. M. Basko, *Nature nanotechnol*, 2013, **8**, 235-246.
35. S. Piscanec, M. Lazzeri, F. Mauri, A. C. Ferrari and J. Robertson, *Physical review letters*, 2004, **93**, 185503-185506.
36. L. M. Malard, M. A. Pimenta, G. Dresselhaus and M. S. Dresselhaus, *Phys Rep*, 2009, **473**, 51-87.
37. A. Gupta, G. Chen, P. Joshi, S. Tadigadapa and P. Eklund, *Nano letters*, 2006, **6**, 2667-2673.
38. C. Casiraghi, S. Pisana, K. S. Novoselov, A. K. Geim and A. C. Ferrari, *Applied physics letters*, 2007, **91**, 233108-233103.
39. E. del Corro, M. Taravillo and V. G. Baonza, *Phys Rev B*, 2012, **85**, 033407-033405.
40. B. Gross, B. Grycz and K. Miklossy, *Plasma technology*, Iliffe Books Ltd, London, 1968.
41. D. A. Gerdeman and N. L. Hecht, *Arc Plasma Technology in Materials Science*, Springer-Verlag, Wien New York, 1972.
42. L. G. Cancado, M. A. Pimenta, B. R. Neves, M. S. Dantas and A. Jorio, *Physical review letters*, 2004, **93**, 247401-247404.
43. C. Casiraghi, A. Hartschuh, H. Qian, S. Piscanec, C. Georgi, A. Fasoli, K. S. Novoselov, D. M. Basko and A. C. Ferrari, *Nano letters*, 2009, **9**, 1433-1441.
44. L. G. Cancado, K. Takai, T. Enoki, M. Endo, Y. A. Kim, H. Mizusaki, A. Jorio, L. N. Coelho, R. Magalhaes-Paniago and M. A. Pimenta, *Applied physics letters*, 2006, **88**, 163106-163103.
45. J. M. Lopes dos Santos, N. M. Peres and A. H. Castro Neto, *Physical review letters*, 2007, **99**, 256802.
46. F. Tuinstra and J. L. Koenig, *The Journal of chemical physics*, 1970, **53**, 1126-1130.
47. L. G. Cancado, A. Jorio, E. Martins Ferreira, F. Stavale and C. A. Achete, *Nano letters*, 2011, **11**, 3190-3196.
48. A. Gupta, Y. Tang, V. H. Crespi and P. Eklund, *Phys Rev B*, 2010, **82**, 241406-241404.
49. V. Carozo, C. M. Almeida, E. H. Ferreira, L. G. Cancado, C. A. Achete and A. Jorio, *Nano letters*, 2011, **11**, 4527-4534.
50. R. Podila, R. Rao, R. Tsuchikawa, M. Ishigami and A. M. Rao, *ACS nano*, 2012, **6**, 5784-5790.

51. F. Banhart, J. Kotakoski and A. V. Krasheninnikov, *ACS nano*, 2011, **5**, 26-41.
52. A. Eckmann, A. Felten, A. Mishchenko, L. Britnell, R. Krupke, K. S. Novoselov and C. Casiraghi, *Nano letters*, 2012, **12**, 3925-3930.
53. D. Nuvoli, L. Valentini, V. Alzari, S. Scognamillo, S. B. Bon, M. Piccinini, J. lllescas and A. Mariani, *J Mater Chem*, 2010, **21**, 3428-3431.
54. J. Dong, B. Zeng, Y. Lan, S. Tian, Y. Shan and X. Liu, *Journal of nanoscience and nanotechnology*, 2010, **10**, 5051-5056.
55. W. Du, J. Lu, P. Sun, Y. Zhu and X. Jiang, *Chem Phys Lett*, 2013, **568-569**, 198-201.
56. L. Zhu, X. Zhao, Y. Li, X. Yu, C. Li and Q. Zhang, *Mater Chem Phys*, 2013, **137**, 984-990.
57. I. K. Moon, J. Lee, R. S. Ruoff and H. Lee, *Nature communications*, 2010, **1**, 626-626.
58. M. Wojtoniszak, X. Chen, R. J. Kalenczuk, A. Wajda, J. Lapczuk and M. Kurzewski, *Colloids and Surface B: Biointerfaces*, 2012, **89**, 79-85.

